



This is a repository copy of *Ongoing intensification of anomalous Western North Pacific anticyclone during post-El Niño summer with achieved carbon neutrality*.

White Rose Research Online URL for this paper:

<https://eprints.whiterose.ac.uk/221266/>

Version: Published Version

Article:

Zhang, W., Tao, W. orcid.org/0000-0002-4629-576X, Huang, G. orcid.org/0000-0002-8692-7856 et al. (5 more authors) (2024) Ongoing intensification of anomalous Western North Pacific anticyclone during post-El Niño summer with achieved carbon neutrality. *npj Climate and Atmospheric Science*, 7 (1). 317. ISSN 2397-3722

<https://doi.org/10.1038/s41612-024-00871-3>

Reuse

This article is distributed under the terms of the Creative Commons Attribution-NonCommercial-NoDerivs (CC BY-NC-ND) licence. This licence only allows you to download this work and share it with others as long as you credit the authors, but you can't change the article in any way or use it commercially. More information and the full terms of the licence here: <https://creativecommons.org/licenses/>

Takedown

If you consider content in White Rose Research Online to be in breach of UK law, please notify us by emailing eprints@whiterose.ac.uk including the URL of the record and the reason for the withdrawal request.



eprints@whiterose.ac.uk
<https://eprints.whiterose.ac.uk/>

<https://doi.org/10.1038/s41612-024-00871-3>

Ongoing intensification of anomalous Western North Pacific anticyclone during post-El Niño summer with achieved carbon neutrality



Wen Zhang^{1,2,9}, Weichen Tao^{1,9} , Gang Huang^{1,2,3} , Kaiming Hu^{1,4,5}, Xia Qu^{1,4}, Ya Wang^{5,6}, Haosu Tang⁷ & Suqin Zhang⁸

Analysis of a suite of global climate model projections under symmetric CO₂ ramp-up and ramp-down (RD) scenarios, our results demonstrate a progressive strengthening of the western North Pacific anticyclone (WNPAC) with rising CO₂ concentrations, a trend that persists as CO₂ declines, followed by gradual recovery without fully returning to its initial state when CO₂ concentrations restore. The overshoot of the WNPAC in the CO₂ RD phase is highly correlated with the enhanced anomalous Maritime Continent (MC) convection, which influences WNPAC through reinforced Kelvin wave response or local Hadley circulation adjustment. This enhanced convection is attributed to increased Indo-Pacific zonal SST gradient associated with strengthened MC warming and accelerated decay of El Niño in the Central Pacific, ultimately linked to climatological equatorial Pacific El Niño-like warming pattern-related air-sea processes. The overshoot of the WNPAC during the CO₂ RD phase may exacerbate flood and high temperature risks in densely populated East Asia.

The boreal summer is a major rainy season for East Asia, where is housing over a billion people and predominantly influenced by the East Asian summer monsoon (EASM). The prominent mode of EASM features a notable anomalous lower-tropospheric anticyclone over the western North Pacific (WNP), generating rapidly in late autumn of El Niño developing year and persisting into the following summer^{1,2}. The WNP anomalous anticyclone (WNPAC) plays a crucial role in modulating El Niño-Southern Oscillation (ENSO)'s impact on summer climate of the East Asia and WNP^{3,4}.

Numerous mechanisms have been proposed to explain the summer-time WNPAC and emphasizes the combined influence of sea surface temperature (SST) anomalies across multiple tropical oceans during El Niño decay phase. Following the peak of El Niño, the tropical Indian Ocean (TIO) warms up and persists into summer due to El Niño-forced atmospheric and oceanic processes^{5–8}. The stimulated eastward Kelvin wave induces Ekman

divergence and suppresses convective processes in the tropical WNP, acting to amplify the anomalous anticyclone^{9–12}. Besides, local cold SST anomalies in the WNP can influence the anticyclone as a Rossby wave response, and a positive thermodynamic feedback is formed between them two and maintained until early summer^{2,13,14}. Additionally, the wind-induced moist enthalpy advection mechanism, driven by enhanced convection over the TIO, transports low moist enthalpy air westward to the WNP, and also contribute to inhibit convection and strengthen the anticyclone in this region¹⁵.

From the perspective of large-scale circulation adjustment, the TIO warming and WNP cooling increase the zonal SST gradient in the Indo-western Pacific, with air converging (diverging) and rising (descending) around the TIO (WNP), favoring the maintenance of the WNPAC^{16–18}. This zonal SST contrast prolong the ENSO's influence on the WNPAC and is known as the Indo-western Pacific Ocean capacitor (IPOC) mode¹⁹. For the

¹State Key Laboratory of Numerical Modeling for Atmospheric Sciences and Geophysical Fluid Dynamics, Institute of Atmospheric Physics, Chinese Academy of Sciences, Beijing, China. ²University of Chinese Academy of Sciences, Beijing, China. ³Laboratory for Regional Oceanography and Numerical Modeling, Qingdao National Laboratory for Marine Science and Technology, Qingdao, China. ⁴Center for Monsoon System Research, Institute of Atmospheric Physics, Chinese Academy of Sciences, Beijing, China. ⁵Key Laboratory of Earth System Numerical Modeling and Application, Institute of Atmospheric Physics, Chinese Academy of Sciences, Beijing, China. ⁶Earth System Numerical Simulation Science Center, Institute of Atmospheric Physics, Chinese Academy of Sciences, Beijing, China. ⁷Department of Geography, University of Sheffield, Sheffield, UK. ⁸Faculty of Geography, Yunnan Normal University, Kunming, China. ⁹These authors contributed equally: Wen Zhang, Weichen Tao. ✉e-mail: tao@mail.iap.ac.cn; hg@mail.iap.ac.cn

cases of fast decaying El Niño, the zonal SST gradient in the Indo-Pacific sector is amplified due to the emergence of warm SST anomalies over the maritime continent (MC) and cold SST anomalies in the central Pacific (CP) during the subsequent summer^{16,20–22}. This SST gradient can enhance the Walker circulation, leading to increased convection around the MC, thereby affecting the WNPAC through a Kelvin wave response or the local Hadley circulation^{16,21,23}.

The increasing Carbon Dioxide (CO₂) concentrations are propelling the climate system towards a severe state, profoundly affecting ecosystems, and human society^{24–26}. Therefore, the Paris Agreement is proposed with the aim to limit global average temperature increase to less than 2 °C above pre-industrial (PI) levels, and pursuing efforts to control temperature increase below 1.5 °C. To achieve this goal, reducing CO₂ emissions by applying carbon dioxide removal (CDR) methods is required^{27–30}. Owing to the ocean's huge heat capacity, particularly in the deep ocean, it accumulates a substantial amount of heat during the CO₂ ramp-up (RU) phase. This heat is redistributed by slow ocean dynamical processes, and then acts on global climate during the CO₂ ramp-down (RD) phase, leading to the hysteresis and irreversibility of climate change. For instance, the global average surface temperature^{31,32}, precipitation^{32–36}, sea level height^{37,38}, sea ice³⁹, and so on, are projected to overshoot, although CO₂ concentrations begin to decline. These fundamental variables can serve as background fields in conjunction with the ocean slow response to influence global main climate system and climate variability, resulting the asymmetrical response of intertropical convergence zones⁴⁰, Hadley circulation^{41,42}, EASM^{43,44}, South Asian summer monsoon^{45,46}, Indian Ocean dipole⁴⁷, ENSO^{48–51}, tropical cyclones⁵², among others. In light of these considerations, it is natural to ask: How does the WNPAC respond during post-El Niño summer under a CDR scenario?

Under global warming scenario, the change of WNPAC remains closely linked to the Indo-Pacific SST anomalies^{53–55}. The amplitude of ENSO generally remains unchanged^{56–58}, while the equivalent ENSO intensity tends to induce stronger TIO SST anomalies due to increased atmospheric moisture⁵⁹, leading to the intensification of WNPAC via amplified tropospheric eastward Kelvin waves^{60,61}. Additionally, the decreased SST anomalies is projected around the CP, indicating the accelerated decay of El Niño, and favors a stronger WNPAC by exciting enhanced Rossby wave response^{55,62}. For the CO₂ RD phase, an investigation conducted by using 28-member ensemble simulations of the CESM1.2 model under an idealized CDR scenario reveals that ENSO variability exhibits substantial increase, which enhances the warm SST anomalies in the TIO and cold SST anomalies in the equatorial central and eastern Pacific (CEP), resulting in the intensification of the WNPAC by exciting atmospheric Kelvin and Rossby wave responses⁴⁹. Nevertheless, their study relies solely on a single model, and the underlying dynamic mechanisms driving changes in the WNPAC, alongside the origins of SST anomalies within tropical basins, remain incompletely understood. In present study, based on nine models from Coupled Model Intercomparison Project Phase 6 (CMIP6), it was found that there is considerable variability in ENSO variability across the models, but the most models exhibit an overshooting phenomenon in the anticyclone. The mechanisms underlying the asymmetric response of WNPAC is investigated under the ideal CO₂ concentration variations, which first increases from PI level at a rate of 1% per year up to four times CO₂ concentrations for 140 years, then decreases symmetrically at the same rate for another 140 years, and finally stabilizes at PI level for 60 years.

Results

Asymmetric response of the WNPAC

Figure 1a shows the regressed SST anomalies, 850-hPa wind anomalies and precipitation anomalies during the June–July–August(1) [JJA(1)] onto the standardized D(0)JF(1) Niño-3.4 index in the CO₂ RU phase. In this study, months within the El Niño developing (decaying) year are marked as 0 and 1, respectively. The anomalous anticyclone in the WNP is well reproduced by most models, as supported by the consistency test. Correspondingly, the entire Indo-Pacific SST anomalies generally exhibit a tri-polar structure, with warm SST anomalies in the TIO and equatorial CP, and weak cold SST

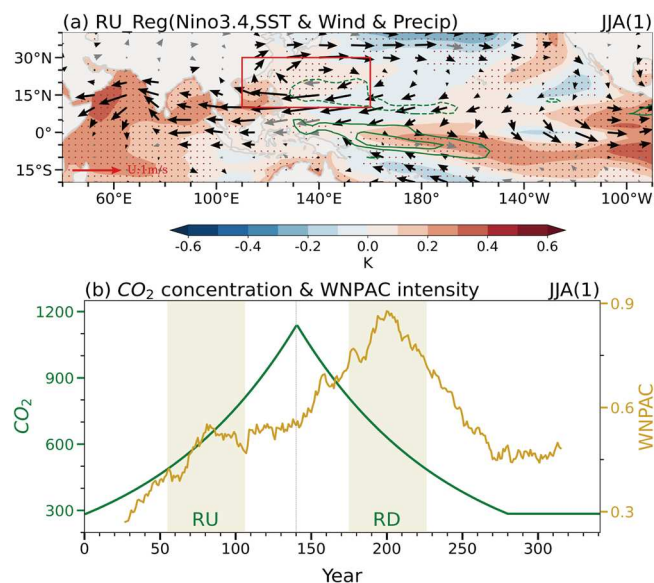


Fig. 1 | The asymmetric response of the WNPAC intensity. **a** Regressed SST anomalies (shading; unit: K), precipitation anomalies (contours; unit: mm day⁻¹), and 850-hPa wind anomalies (vectors; unit: m s⁻¹) during JJA(1) onto the standardized D(0)JF(1) Niño-3.4 index in the CO₂ RU period for 9 models' MME. For precipitation anomalies, solid contours represent positive values at 0.6 and 1.2 mm day⁻¹, while dashed contours indicate negative values at -0.6 and -1.2 mm day⁻¹. The black arrows and brown dots denote that at least 70% of models show consistent results. The red solid line rectangle highlights the WNPAC region. **b** Evolution of CO₂ concentrations (unit: ppm) and WNPAC intensity (unit: 10⁻⁶ s⁻¹) for 9 models' MME. The WNPAC intensity is defined as the negative of the area-averaged vorticity anomalies. The green shadings correspond to the selected CO₂ RU (55–105) and RD (175–225) period. The dashed vertical lines indicate the year 140, when CO₂ concentrations peak.

anomalies in the WNP, indicating that the models can reasonably capture the impact of the IPOC mode on the WNPAC during the ENSO decay phase (Fig. S1). However, some discrepancies with observations are noted: the models fail to reproduce the SST warming in the eastern Indian Ocean, overestimate the positive precipitation anomalies in the equatorial CP, and underestimate the positive (negative) precipitation anomalies in the TIO (WNP) (Figs. 1a and 7 in ref. 19).

The negative regional mean vorticity of the 850-hPa wind anomalies in the WNP region (10°–30°N, 110°–160°E, encircled area in Fig. 1a) is calculated to represent the intensity of the WNPAC, and the timeseries of the WNPAC in 9 models' multi-model ensemble (MME) and the associated variation of CO₂ concentrations are depicted in Fig. 1b. Despite the inter-annual fluctuations in the time series of WNPAC with the increase of CO₂ concentrations, WNPAC still trends towards intensification, which is consistent with the conclusion drawn under CMIP6 SSP5-8.5 scenario⁵⁴. However, when the CO₂ concentrations begin to decrease, the intensity of the WNPAC shows an overshoot phenomenon, and the intensification continues until around the 200th year, followed by a gradual recovery. The WNPAC does not return to the initial intensity when CO₂ concentrations revert to PI level. We also try calculating the WNPAC intensity by using another definition¹², and the results are consistent with those obtained by using the regional vorticity average (figure not shown).

The time series of the WNPAC intensity in each model are displayed in Fig. S2. To minimize the impact of individual model, the MME results are verified by recalculating after excluding individual models, and the asymmetric features remain robust (Fig. S3). Due to internal variability across models, there are some differences in the time series of WNPAC changes. To further verify the reliability of the 9 models' MME results, the trajectories of WNPAC intensity under entire pathway of CO₂ concentrations in each model are examined in Fig. S4. For the same CO₂ concentrations, seven

models show a stronger WNPAC during the CO₂ RD compared to RU phase in most instances. These seven models exhibit a distinct pattern of initial strengthening followed by subsequent weakening during the CO₂ RD phase, indicating a pronounced overshooting and asymmetric response of the WNPAC. Additionally, we provide the horizontal distributions of 850-hPa wind and vorticity anomalies over the WNP region for the differences between nine pairs of periods starting from years 1–51 (230–280) of the RU (RD) phase with 10-year intervals until years 81–131 (150–200) (Fig. S5). Consistency tests show that at least seven models successfully simulate the anticyclonic anomalies and negative vorticity anomalies in each time period, reinforcing the reliability of the asymmetric response identified in the WNPAC.

Causes of the WNPAC's asymmetric response

To elucidate the asymmetric response of the WNPAC intensity, the years from 175 to 225, when exhibit the strongest intensity, are selected as the CO₂ RD period, and the years from 55 to 105 having equivalent CO₂ concentrations with the CO₂ RD period are selected as the CO₂ RU period. The differences in regressed variable fields between the two periods are presented in Fig. 2a. An anomalous anticyclone appears over the WNP, indicating that the WNPAC is intensified during the RD period compared to the RU period, consistent with the conclusions of WNPAC time series in Fig. 1b. For the differences of regressed precipitation anomalies, in addition to the enhanced dry anomalies in the WNP corresponding with the intensified WNPAC, wet anomalies emerge from the central TIO to MC, particularly pronounced for the latter region. The anomalous SST differences are characterized by weak warm anomalies from the central TIO to MC and cold anomalies in the equatorial CP, thereby increasing the zonal SST gradient over the Indo-Pacific sector.

As reviewed in the Introduction, the enhanced zonal SST gradient could strengthen the Walker circulation, resulting in increased convection around the MC, which further strengthens the WNPAC through a Kelvin wave response or the local Hadley circulation adjustment^{16,20,23}. Moreover, the increased negative precipitation anomalies over the tropical WNP (Fig. 2a) may directly reinforce the anticyclone as a Rossby wave response^{15,63,64}. Besides, changes in ENSO variability does not consistently impact WNPAC across 9 models (Fig. S6), as revealed by findings in ref. 49. 7 out of 9 models show very low or even negative correlation coefficients between them two, similar to previous conclusions obtained by reanalysis datasets^{17,21,65}. It indicates that variations in the WNPAC intensity may not directly depend on changes of ENSO variability. In the next subsection, the mechanisms involved in the enhanced positive precipitation anomalies in the MC and negative precipitation anomalies in the tropical WNP, as well as their contributions to the overshooting of the WNPAC, are investigated.

Formation and impact of MC precipitation changes. Figure 2b illustrates the meridional mean (10°S–5°N) of zonal circulation anomalies. Coupled with the warm and cold SST anomalies in the Indo-Pacific sector, there is a wide range of upward motions over the tropical TIO and MC, and the CP are dominated by downward motions. The strongest upward anomalies occur around 500-hPa over the MC, and the strongest downward anomalies are centered at 250-hPa over the CP. Together, these anomalies form a complete zonal circulation system, which indicates the enhancement of the Walker circulation and promotes positive precipitation anomalies over the MC. Notably, the upward motions over the MC corresponds to the clear positive precipitation anomalies (Fig. 2a, b), while the downward motions over the CP does not lead to a significant negative precipitation anomalies. This is because that the subsidence over the CP primarily occurring at the upper-level has a limited impact on moisture distribution and convection in the lower atmosphere^{2,66}.

To investigate the evolution of the MC precipitation, we focus on the region with the strongest positive precipitation anomalies (red dashed lines encircled area in Fig. 2a). The timeseries show a gradual increase in these anomalies during the CO₂ RU phase, with the peak occurring around year

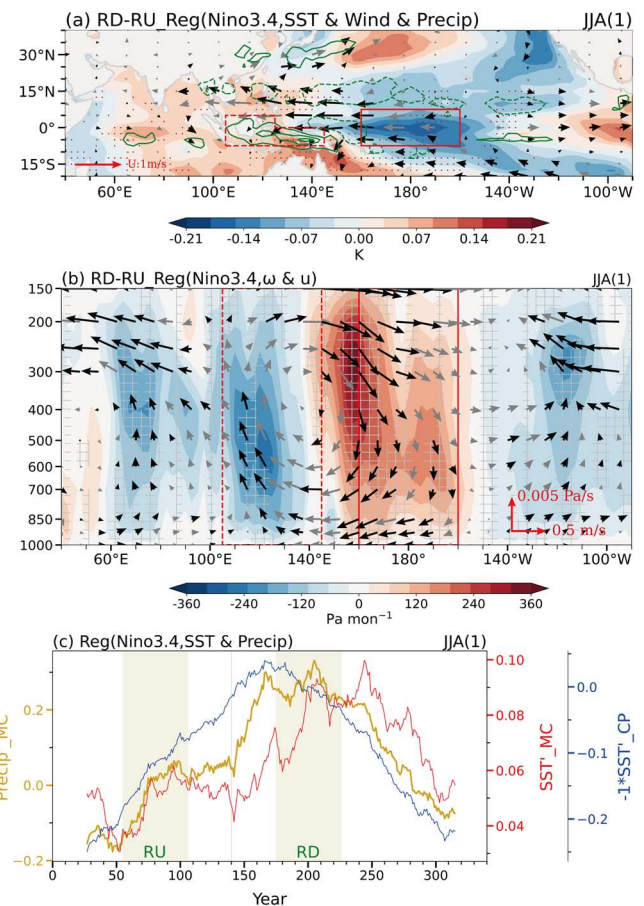


Fig. 2 | The increased convection around the MC and its underlying causes.

a Regressed SST anomalies (shading; unit: K), precipitation anomalies (contours; unit: mm day⁻¹), and 850-hPa wind anomalies (vectors; unit: m s⁻¹) during JJA(1) onto the standardized D(0)JF(1) Niño-3.4 index in the differences between the CO₂ RD and RU period for 9 models' MME. For precipitation anomalies, solid contours represent positive values at 0.3 and 0.6 mm day⁻¹, while dashed contours indicate negative values at -0.3 and -0.6 mm day⁻¹. **b** Regressed meridional mean (10°S–5°N) vertical pressure velocity anomalies (shading; unit: Pa day⁻¹) and wind anomalies (arrows; units: Pa s⁻¹ and m s⁻¹) during JJA(1) onto the standardized D(0)JF(1) Niño-3.4 index in the differences between the CO₂ RD and RU period for 9 models' MME. The brown dots in (a), gray grids in (b), and black arrows in (a), (b) denote that at least 70% models show consistent results. The red solid line rectangles in (a), (b) highlight the equatorial CP region, and the red dashed line rectangles highlight the MC region. **c** Evolution of the regressed precipitation anomalies in the MC (yellow line; unit: mm day⁻¹), SST anomalies in the equatorial CP (red line; unit: K), and SST anomalies in the MC (blue line; unit: K) during JJA(1) onto the standardized D(0)JF(1) Niño-3.4 index for 9 models' MME. The green shadings correspond to the selected CO₂ RU (55–105) and RD (175–225) period. The dashed vertical lines indicate the year 140, when CO₂ concentrations peak.

200 during the CO₂ RD phase, followed by a slow decline (Fig. 2c). Three regions of SST anomalies are examined to explore their potential relationship with MC precipitation anomalies, including the warm SST anomalies in the TIO (20°S–10°N, 60°E–90°E), the MC (10°S–5°N, 105°E–125°E, and 10°S–0°, 125°E–145°E; red dashed lines encircled area in Fig. 2a), and the cold SST anomalies in the CP (160°E–160°W; red solid lines encircled area in Fig. 2a). The SST anomalies in the TIO, as shown in Fig. S7, exhibit minimal variability and no robust asymmetric response, excluding their contribution to the convection changes over the MC. The SST anomalies in both the MC and equatorial CP show a delayed response relative to CO₂ concentration changes, with their peak values occurring approximately 30 years before and after the peak of the MC precipitation anomalies, respectively (Fig. 2c). This temporal alignment suggests a joint contribution to the

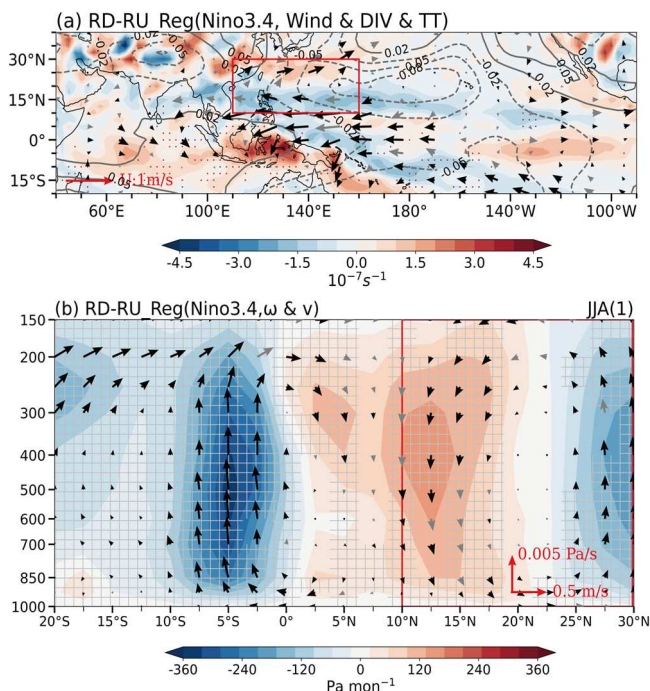


Fig. 3 | Physical processes associated with how increased convection around the MC influences the WNPAC. a Regressed negative 925-hPa divergence anomalies (shading; unit: 10^{-7} s^{-1}), 925-hPa wind anomalies (vectors; unit: m s^{-1}), and vertically averaged (850–200 hPa) air temperature anomalies (contours; unit: K) during JJA(1) onto the standardized D(0)JF(1) Niño-3.4 index in the differences between the CO₂ RD and RU period for 9 models' MME. The air temperature anomalies are adjusted by subtracting the mean value across the entire tropics (20°S–20°N, 180°W–180°E). The red solid line rectangles highlight the tropical WNP region. **b** Regressed zonal mean (105°E–145°E) vertical pressure velocity anomalies (shading; unit: Pa day^{-1}) and wind anomalies (arrows; units: Pa s^{-1} and m s^{-1}) during JJA(1) onto the standardized D(0)JF(1) Niño-3.4 index in the differences between the CO₂ RD and RU period for 9 models' MME. The red solid line rectangles highlight the tropical WNP region. The brown dots in (a), gray grids in (b), and black arrows in (a), (b) denote that at least 70% models show consistent results.

MC precipitation anomalies, a conclusion further supported by individual model results (Fig. S8).

Notably, the MC warming is relatively weaker than the equatorial CP cooling (Fig. 2a). However, the MC region, characterized by higher climatological SST along with more vigorous convection activities, is susceptible to induce convection and precipitation anomalies even with minor local temperature perturbations.

On one hand, the MC warming and enhanced precipitation further amplify the eastward Kelvin waves penetrating into the western Pacific (Fig. 3a). The Kelvin wave-induced easterly anomalies decrease with increasing latitude, leading to negative relative vorticity anomalies over the WNP. These anticyclonic vorticity at the upper boundary layer, which initiates boundary layer divergence through the Ekman pumping process as shown in Fig. 3a, inhibiting local convection and sustaining the WNPAC^{10,11}.

On the other hand, in the zonal mean of meridional circulation anomaly fields, the enhanced convection over the MC strengthens the ascending branch centered around 5°S and the corresponding descending motions centered near 12.5°N, forming an anomalous local Hadley circulation and reinforcing the WNPAC (Fig. 3b). The time series of MC precipitation anomalies confirm its close relationship with WNPAC, as both time series present the asymmetric characteristics and peak around year 200, and the correlation coefficient between them reaches at 0.92 (Figs. 1b and 2c). These mechanisms align with previous studies, which mention the enhanced convection around the MC could influence the WNPAC via Kelvin wave-induced Ekman divergence^{9–12} or adjustments of the local Hadley circulation^{16,21,23}.

Formation and impact of WNP precipitation changes. Moisture budget analysis is used to examine the WNP region (5°–20°N, 140°E–170°E; encircled area in Fig. 4c), where negative precipitation anomalies are most prominent (Fig. 2a) and can reinforce the WNPAC as a Rossby wave response^{15,63,64}. The results show that the reduction in precipitation anomalies is primarily driven by climatological moisture advection due to enhanced subsidence anomalies ($-\langle \Delta \omega' \cdot \partial_p q \rangle$; Fig. 4a), and the role of changes in subsidence anomalies is dominant⁶⁷. In the tropics, these vertical motion anomalies are constrained by the moist static energy (MSE) budget. The climatological MSE advection due to enhanced subsidence anomalies ($\langle \Delta \omega' \cdot \partial_p h \rangle$) in the WNP is primarily balanced by climatological horizontal advection of changed anomalous moist enthalpy ($-\langle \vec{u} \cdot \nabla_h (\Delta s') \rangle$; Fig. 4b). The spatial distribution of each term in the MSE equation is depicted in Fig. S9.

For $-\langle \vec{u} \cdot \nabla_h (\Delta s') \rangle$, the strongest negative anomalies are found at the 925-hPa boundary layer (figure not shown). At this level, the WNP region experiences climatological easterly winds, which transport anomalous negative moist enthalpy into the area (Fig. 4c), stabilizing the atmospheric column and suppressing convection. This reduction in anomalous moist enthalpy in boundary layer is linked to cooling changes in SST anomalies⁶⁴. The cold SST anomalies, located on the northern flank of the equatorial CP and associated with the rapid decay of El Niño, suppress boundary layer moisture and atmospheric temperature anomalies, leading to a decrease in anomalous moist enthalpy during the CO₂ RD compared to RU period. Although the peak of $-\langle \vec{u} \cdot \nabla_h (\Delta s') \rangle$ does not coincide directly with precipitation anomalies, this dynamic term exhibits a notable slowdown in the recovery during the CO₂ RD phase (Fig. 4d). This delayed recovery plays a significant role in the lagged response of WNP precipitation anomalies.

In summary, during the CO₂ RD period, enhanced warm SST anomalies over the MC and cold SST anomalies in the equatorial CP increase the zonal SST gradient across the Indo-Pacific, which boosts convection around the MC and strengthens the WNPAC via Kelvin wave-induced Ekman divergence^{9–12} or adjustments of the local Hadley circulation^{16,21,23}. Additionally, the cold SST anomalies in the equatorial CP result in negative moist enthalpy anomalies in the northern boundary layer, which are transported by the climatological easterlies, suppress convection over the tropical WNP and further enhance the anticyclone as a Rossby wave response^{15,63,64}. To better understand the causes of the increased zonal SST gradient, subsequent research will be directed towards elucidating the physical processes behind the delayed response of SST anomalies in the equatorial CP and MC.

Origin of asymmetric SST anomalies in the equatorial CP

Figure 5a shows that the decay rate of SST anomalies over the equatorial CP after the end of the ENSO mature winter intensifies with the increase of CO₂ concentrations, persisting until around the 170th year in the CO₂ RD phase. This accelerated decay of warm SST anomalies is consistent with the time evolution characteristic of equatorial CP SST anomalies during JJA(1) (Fig. 2c). To investigate the mechanisms behind the asymmetric response of SST anomalies in the equatorial CP, the mixed-layer temperature tendency equation is employed in this section, and we analyze the involved key physical processes and their working months. The change of mixed-layer temperature is governed by thermodynamic and dynamic processes. The former encompasses the roles of net surface shortwave radiation (SWR), net surface longwave radiation (LWR), sensible heat flux (SHF), and latent heat flux (LHF), and the latter involves oceanic advection processes and advection feedback processes.

For the evolution of mixed-layer temperature tendency anomalies ($\partial T' / \partial t$) in the equatorial CP, two distinct accelerated decay periods are observed in late winter [JF(1)] and early summer [MJ(1)] (Fig. 6a). Moreover, the accelerated decay exhibits the delayed recovery in both periods, cumulatively leading to the asymmetric response of equatorial CP SST anomalies during JJA(1). It is important to note that although the mixed-layer temperature tendency anomalies peak around year 145 during JF(1) (Fig. 6c) and does not align perfectly with the WNPAC (Fig. 1b) or

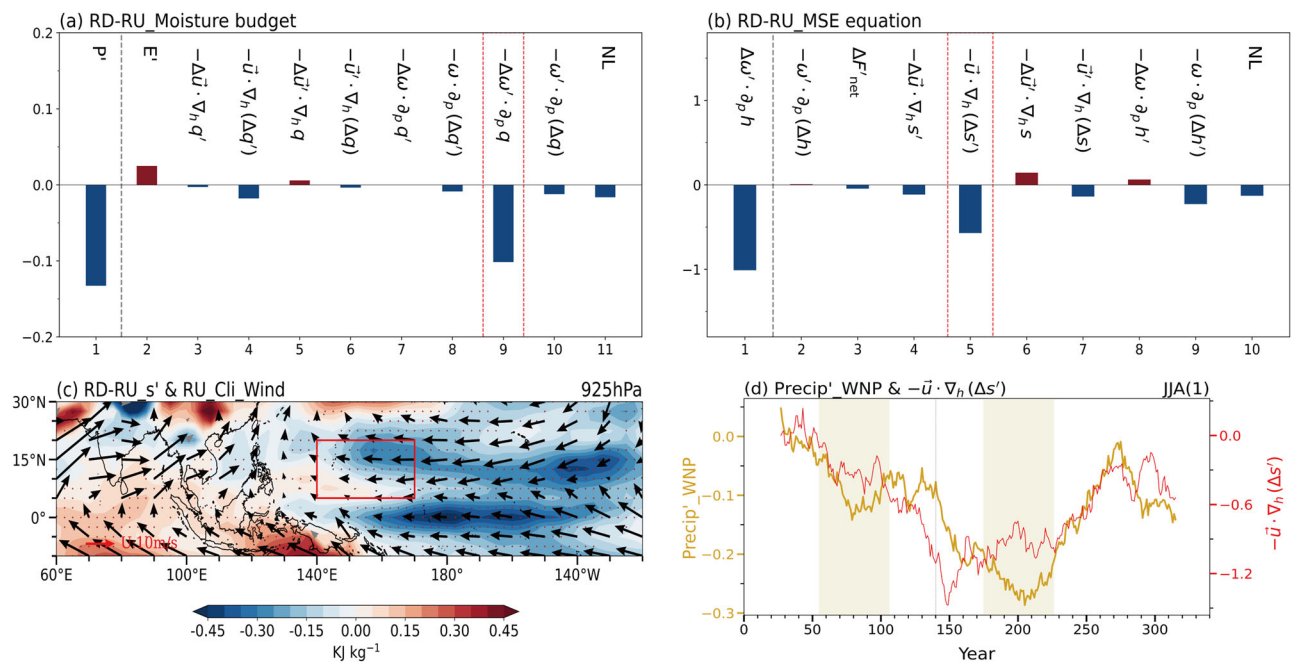


Fig. 4 | The role of the wind-induced moist enthalpy advection mechanism. **a** Moisture budget (mm day⁻¹) over the tropical WNP within regions of pronounced negative precipitation anomalies in the differences between the CO₂ RD and RU period for 5 models' MME. **b** Same as (a), but the MSE budget (W m⁻²). The red dashed line rectangles in (a), (b) highlight the processes with the greatest contributions. **c** The 925-hPa climatological winds (vectors; unit: m s⁻¹) during JJA(1) in the CO₂ RU period, and regressed 925-hPa moist enthalpy anomalies (shading; kJ kg⁻¹) during JJA(1) onto the standardized D(0)JF(1) Niño-3.4 index in the differences between the CO₂ RD and RU period for 5 models' MME. The brown dots and

black arrows denote that at least 70% models show consistent results. The red solid line rectangle highlights the tropical WNP within regions of pronounced negative precipitation anomalies. **d** The evolution of regressed precipitation anomalies (yellow line; unit: mm day⁻¹) onto the standardized D(0)JF(1) Niño-3.4 index and $-\langle \bar{u} \cdot \nabla_h (\Delta s') \rangle$ (red line; unit: W m⁻²) in the tropical WNP during JJA(1) for 5 models' MME. The green shadings correspond to the selected CO₂ RU (55–105) and RD (175–225) period. The dashed vertical lines indicate the year 140, when CO₂ concentrations peak. The prime symbols in (c), (d) represent the anomalies caused by ENSO.

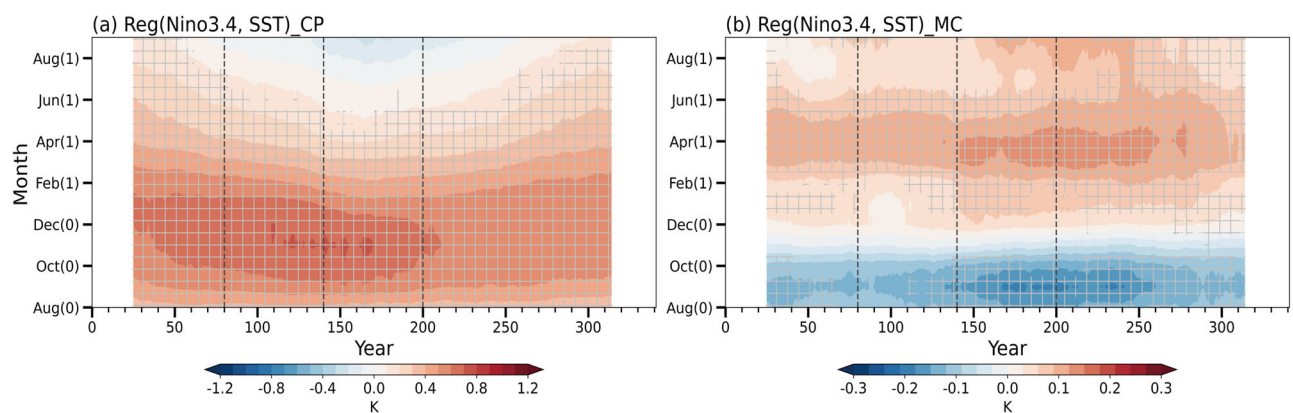


Fig. 5 | Changes of SST anomalies in the equatorial CP and MC. **a** Hovmöller diagrams of regressed SST anomalies (unit: K) in the equatorial CP onto the standardized D(0)JF(1) Niño-3.4 index for 9 models' MME. **b** Same as (a), but in the MC.

The gray grids denote the region in which at least 70% models show consistent results. The dashed vertical lines respectively denote the central year of RU period, the peak year of CO₂ concentrations, and the central year of RD period.

equatorial CP SST anomalies (Fig. 2c), the recovery during the CO₂ RD phase is slower, contributing to the delayed recovery of the equatorial CP SST anomalies. The mixed-layer temperature tendency equation effectively reproduces the main characteristics of mixed-layer temperature anomalies in the equatorial CP, with delayed recovery of two accelerated decay periods (Fig. 6b). The detailed contributions from each thermodynamic and dynamic component are presented in Fig. S10.

Furthermore, attention is directed towards identifying the dominant physical processes driving mixed-layer temperature anomalies in the two periods. During JF(1), the reductions in SWR and LHF anomalies accelerate

the decay of equatorial CP SST anomalies (Fig. S10a and d). During MJ(1), the mean meridional advection of the anomalous temperature gradient ($-\bar{v} \partial T' / \partial y$) emerges as the primary contributor and hastens the decay (Fig. S10h). Subsequent analysis will delve into elucidating the reasons behind the asymmetric response of these three processes.

Anomalous SWR in JF(1). During the JF (1) period, an asymmetric response can be seen in the time series of SWR anomalies (Figs. 6c and S10a). In the tropics, SWR tends to co-vary with cloud cover^{68,69}. By comparing these anomalies between the total SWR and clear-sky SWR to

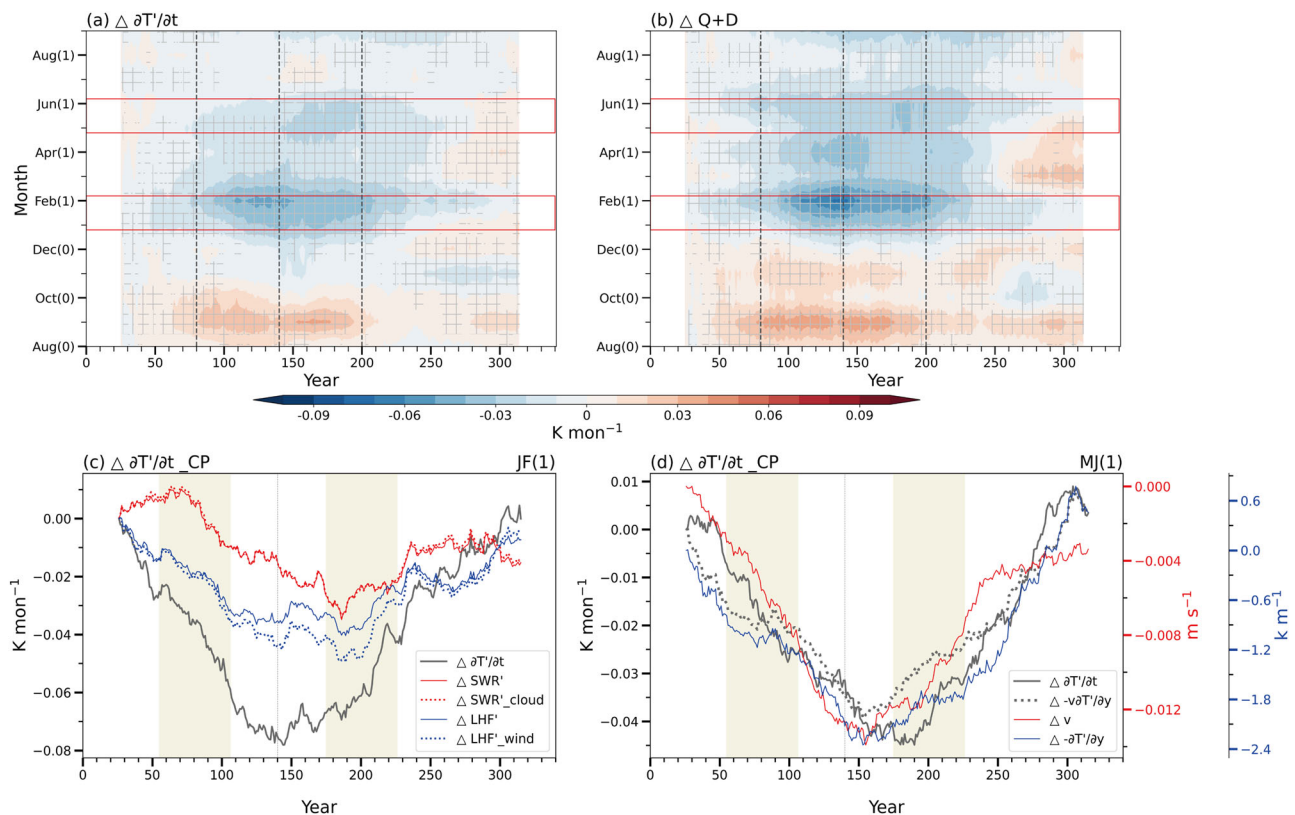


Fig. 6 | The critical periods and physical processes for the accelerated decay of the SST anomalies in the equatorial CP. **a** Hovmöller diagrams of the mixed-layer temperature tendency anomalies ($\partial T' / \partial t$) in the equatorial CP (unit: K month^{-1}) for 5 models' MME. The $\partial T' / \partial t$ values are calculated as the difference in temperature anomalies between times t and $t - 1$. The difference term, $\Delta \partial T' / \partial t$, is calculated by subtracting the result of the initial period of the CO_2 RU phase. **b** Same as (a), but the combined contributions of thermodynamic and dynamic processes from mixed-layer temperature tendency equation. The gray grids in (a), (b) denote the region in which at least 70% models show consistent results. The dashed vertical lines in (a), (b) respectively denote the central year of RU period, the peak year of CO_2 concentrations, and the central year of RD period. The red solid line rectangles in (a), (b) highlight the critical periods. **c** Evolution of mixed-layer temperature tendency anomalies in the equatorial CP during JF(1) (grey solid line; units: K month^{-1}), the contribution of SWR anomalies (red solid line; units: K month^{-1}), the contribution

of SWR anomalies related to cloud (red dashed line; units: K month^{-1}), the contribution of LHF anomalies (blue solid line; units: K month^{-1}), and the contribution of LHF anomalies related to wind speed (blue dashed line; units: K month^{-1}) for 5 models' MME. **d** Evolution of mixed-layer temperature tendency anomalies in the equatorial CP during MJ(1) (grey solid line; units: K month^{-1}), the contribution of mean meridional advection of anomalous temperature gradient ($-\bar{v} \partial T' / \partial y$; grey dashed line; units: K month^{-1}), mean meridional ocean currents (\bar{v} ; red solid line; units: m s^{-1}), and meridional gradient of temperature anomalies ($-\partial T' / \partial y$; blue solid line; units: K m^{-1}) for 5 models' MME. The green shadings in (c), (d) correspond to the selected CO_2 RU (55–105) and RD (175–225) period. The dashed vertical lines in (c), (d) indicate the year 140, when CO_2 concentrations peak. The prime symbols represent the anomalies caused by ENSO. The Δ symbols represent the deviation relative to the initial period of the CO_2 RU phase.

isolate the contribution of cloud cover, and the obtained time series of SWR anomalies related to cloud indicate a high degree of synchronization with the time series of total SWR anomalies, demonstrating that the changes in cloud cover predominantly induce the anomalous SWR (Fig. 6c).

Cloud formation is closely linked to convective activities^{70,71}. In the CO_2 RU period, the entire equatorial Pacific exhibits positive precipitation anomalies in response to El Niño, particularly pronounced in the tropical CP (Fig. 7a). The disparity between the RD and RU period shows an intensification of precipitation anomalies in the equatorial CEP, and a decrease in the western Pacific (Fig. 7b). Especially for the equatorial CP region, an obvious increase in precipitation anomalies is observed, leading to a reduction of SWR into ocean surface, thereby favoring the accelerated decay of local SST during the JF(1) period. However, similar to previous conclusions, the changes of El Niño-related SST anomalies are not evident^{56–58} (Fig. S11b).

Beside the role of SST anomalies, the tropical precipitation response is also modulated by the climatological SST background⁶⁷. The climatological SST differences between the RD and RU period suggest an El Niño-like warming in the equatorial Pacific (Fig. 7b), which is similar to the results projected by CMIP models under various global warming scenarios^{72–74}.

According to a simplified moisture budget decomposition, ref. 67 found that the changes of precipitation anomalies are primarily controlled by the dynamic component related to the changes in ENSO-driven vertical motions. Under the climatological equatorial Pacific El Niño-like SST warming, the substantial increase in low-level specific humidity over the equatorial CEP weakens atmospheric stability, leading to an intensification and eastward shift of the ENSO-induced circulation anomalies and consequently the precipitation response. Therefore, the asymmetric response of SWR anomalies under CDR scenario can be fundamentally attributed to climatological equatorial Pacific warming pattern.

Anomalous LHF in JF(1). LHF variations result from atmospheric forcing and oceanic response, with atmospheric forcing encompassing contributions from wind speed, relative humidity, and sea-air temperature difference. The changes of LHF anomalies in the equatorial CP region stem from the atmospheric forcing (Fig. S12a and c), and the wind-induced LHF anomalies emerge as the dominant contribution (Fig. S12e). Moreover, the time series of LHF anomalies and corresponding wind-induced LHF anomalies over the equatorial CP are examined (Fig. 6c), they exhibit a high degree of consistency. As that both the influence of changes in climatological and anomalous wind speed are included in the

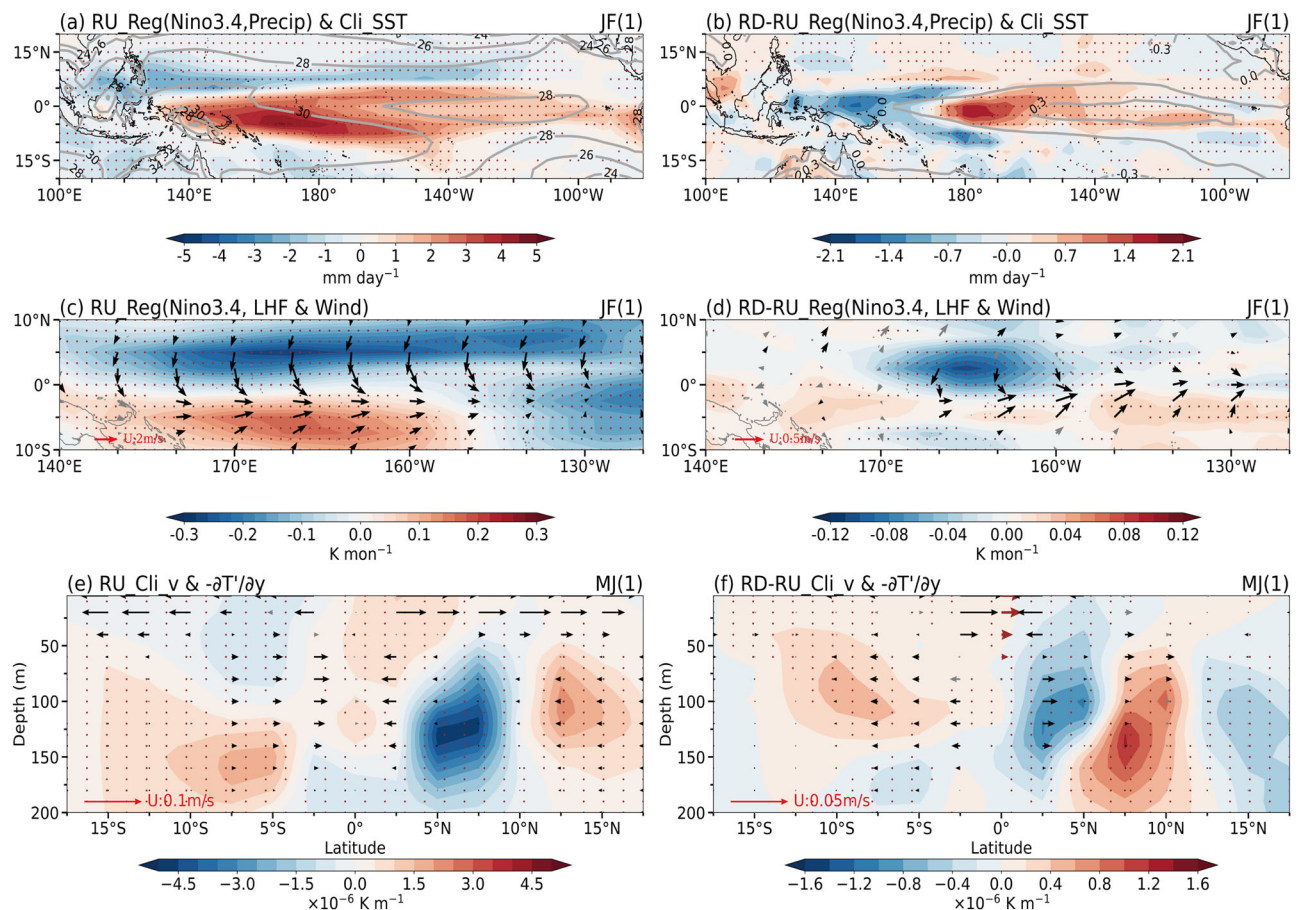


Fig. 7 | The spatial fields corresponding to the key physical processes of the equatorial CP. a Climatological mean SST (contours; unit: °C) during JF(1) and regressed precipitation anomalies (shading; unit: mm day⁻¹) during JF(1) onto the standardized D(0)JF(1) Niño-3.4 index in the CO₂ RU period for 5 models' MME. **b** Same as (a), but for the differences between the CO₂ RD and RU period. The climatological mean SST is adjusted by subtracting the mean value across the entire tropics (20°S–20°N, 180°W–180°E). **c** Regressed LHF anomalies (shading; unit: K month⁻¹) and 1000-hPa wind anomalies (vectors; unit: m s⁻¹) during JF(1) onto the standardized D(0)JF(1) Niño-3.4 index in the CO₂ RU period for 5 models' MME.

d Same as (c), but for the differences between the CO₂ RD and RU period. **e** The zonal average (160°E–160°W) of the climatological mean meridional ocean currents (\bar{v} ; vectors; unit: m s⁻¹) and the meridional gradient of mixed-layer temperature anomalies ($-\partial T'/\partial y$; shading; unit: K m⁻¹) in the CO₂ RU period for 5 models' MME. **f** Same as (e), but for the differences between the CO₂ RD and RU period and the climatological mean meridional ocean currents at the equator is indicated by brown arrows. The prime symbols in (e), (f) represent the anomaly caused by ENSO. The black arrows and brown dots denote that at least 70% models show consistent results.

calculation of wind-induced LHF anomalies, further decomposition is conducted to reveal their relative importance (Fig. S13), and the results show that the contribution of wind speed anomalies is dominant (Fig. S13b).

During the CO₂ RU period, when an El Niño event occurs, warm SST anomalies emerge in the equatorial CEP (Fig. S11a), corresponding to the convergence of lower-level wind anomalies (Fig. 7c). To the north (south) of the equator, the anomalous northerly (westerly) winds combine with the climatological northeasterly (southeasterly) winds, enhancing (reducing) evaporation and resulting in negative (positive) LHF anomalies (Figs. 7c and S11a). In the CO₂ RD period, accompanied with the intensification of precipitation anomalies over the equatorial CP (Fig. 7b), the anomalous northerly winds in the north are strengthened, consequently amplifying the negative LHF anomalies within this region (Fig. 7d). As previously discussed, the increased precipitation anomalies are fundamentally linked to the climatological equatorial Pacific warming.

Meridional advection of anomalous temperature in MJ(1). During the MJ(1) period, the mean meridional advection of anomalous temperature gradient ($-\bar{v}\partial T'/\partial y$) dominantly contributes to the asymmetric response in mixed-layer temperature decay (Figs. 6d and S10h). This asymmetry is

intricately related to both the mean meridional ocean currents (\bar{v}) and the meridional gradient of mixed-layer temperature anomalies ($-\partial T'/\partial y$) (Fig. 6d). The equatorial CP, typically governed by climatological easterlies, features northward (southward) meridional ocean currents north (south) of the equator via Ekman transport (Fig. 7e). Simultaneously, due to that the warm SST anomalies are closer to the equator in this region, the meridional gradients of mixed-layer temperature anomalies manifest as positive (negative) values to the north (south) near the equator (Fig. 7e). Thus, the resulting warm meridional advection favors the maintenance of warm SST anomalies over the CP.

During the CO₂ RD period, the mixed-layer meridional current differences show a trend of convergence toward the equator relative to the CO₂ RU period, indicating a weakening of climatological meridional currents (Figs. 6d and 7f). This weakening can be attributed to the diminished easterlies in the equatorial CP due to the climatological equatorial Pacific warming pattern^{73,76}. Furthermore, the accelerated dissipation of SST anomalies in the equatorial CP leads to a decrease in the absolute value of the meridional gradient of mixed-layer temperature anomalies on both sides of the equator (Figs. 6d and 7f). The concurrent weakening of meridional ocean currents and the meridional gradient of mixed-layer temperature anomalies collectively diminishes the warm advection and accelerates the decay of equatorial CP SST anomalies.

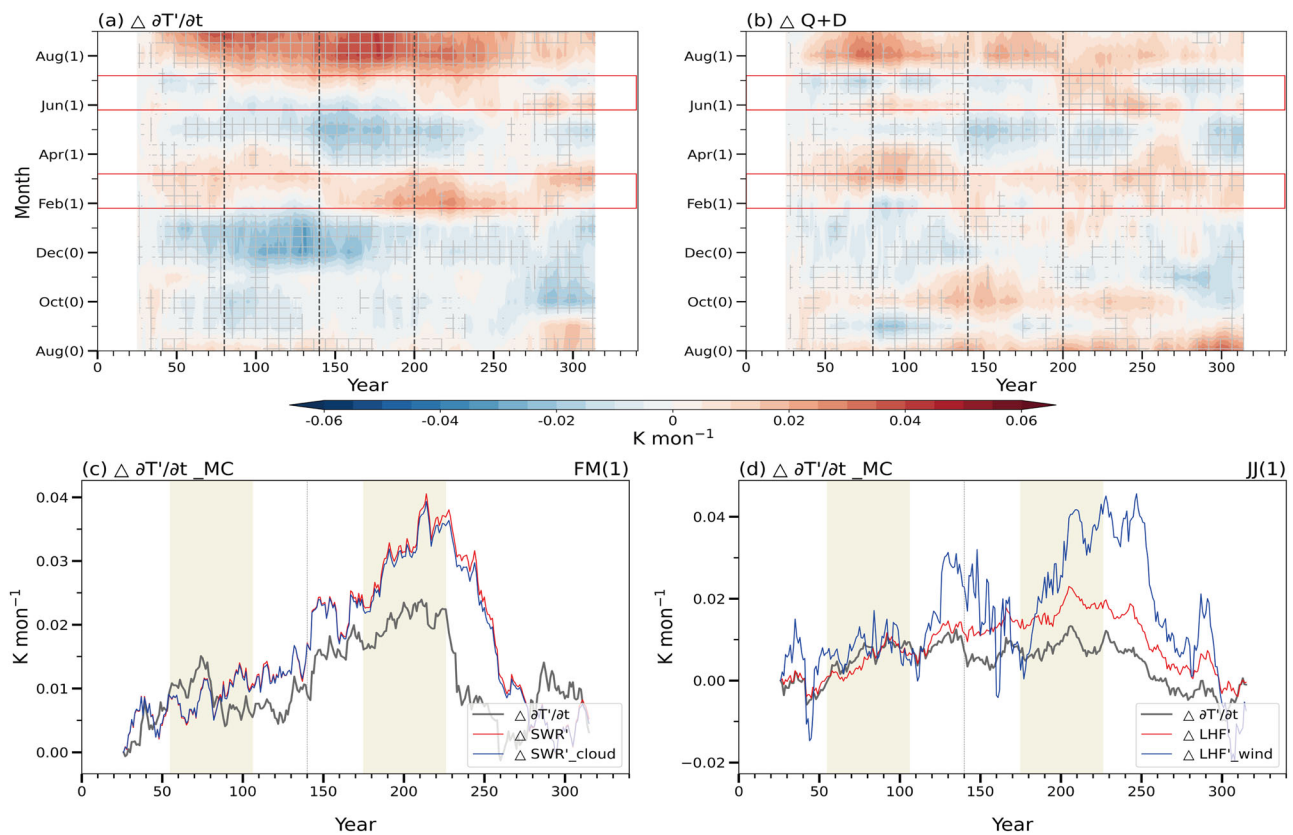


Fig. 8 | The critical periods and physical processes for the strengthened warming of the SST anomalies in MC. **a** Hovmöller diagrams of the mixed-layer temperature tendency anomalies in the MC (unit: K month⁻¹) for 5 models' MME. The $\partial T'/\partial t$ values are calculated as the difference in temperature anomalies between times t and $t - 1$. The difference term, $\Delta \partial T'/\partial t$, is calculated by subtracting the result of the initial period of the CO₂ RU phase. **b** Same as (a), but the combined contributions of thermodynamic and dynamic processes from mixed-layer temperature tendency equation. The gray grids in (a), (b) denote the region in which at least 70% models show consistent results. The dashed vertical lines in (a), (b) respectively denote the central year of RU period, the peak year of CO₂ concentrations, and the central year of RD period. The red solid line rectangles in (a), (b) highlight the critical periods. **c** Evolution of mixed-layer temperature tendency anomalies in the MC during

FM(1) (grey solid line; units: K month⁻¹), the contribution of SWR anomalies (red solid line; units: K month⁻¹), and the contribution of SWR anomalies related to cloud (blue solid line; units: K month⁻¹) for 5 models' MME. **d** Evolution of mixed-layer temperature tendency anomalies in the MC during JJ(1) (grey solid line; units: K month⁻¹), the contribution of LHF anomalies (red solid line; units: K month⁻¹), and the contribution of LHF anomalies related to wind speed (blue solid line; units: K month⁻¹) for 5 models' MME. The green shadings in (c), (d) correspond to the selected CO₂ RU (55–105) and RD (175–225) period. The dashed vertical line in (c), (d) indicates year 140, when CO₂ concentrations peak. The prime symbols represent the anomaly caused by ENSO. The Δ symbols represent the deviation relative to the initial period of the CO₂ RU phase.

Origin of asymmetric SST anomalies in the MC

The positive SST anomalies in the MC region develop from ENSO mature winter and reach a warming peak in the following spring, followed by a secondary warming from July(1) (Fig. 5b). The asymmetric response to the changes of CO₂ concentrations coincidentally corresponds to two warming peaks. The mixed-layer temperature tendency indicates that the strengthened JJA(1) MC warming in CO₂ RD phase is mainly associated with two periods: early spring (FM(1)) and early summer (JJ(1)) (Fig. 8a). The results derived from mixed-layer temperature tendency equation accurately capture the features of original temperature tendency, as well as the asymmetric response during the two pivotal periods (Fig. 8b–d). In comparison with thermodynamic processes, oceanic dynamic processes exhibit negligible influence on the changes in the MC mixed-layer temperature evolution (Fig. S14). Specifically, the FM(1) and JJ(1) period are primarily linked to an increase in SWR (Figs. S14a and 8c) and LHF anomalies (Figs. S14d and 8d), respectively.

Anomalous SWR in FM(1). In the FM(1) period, the precipitation anomalies are similar to those in the JF(1) period (Figs. 7a and 9a), characterized by positive precipitation responses in the tropical Pacific region and negative precipitation responses in the MC region. The climatological equatorial Pacific warming pattern induce an uneven

increase in lower-level specific humidity, thereby engendering structural changes in the circulation and precipitation anomalies⁶⁷. Relative to the CO₂ RU period, the CO₂ RD period experiences the enhanced ENSO-related precipitation anomalies in the equatorial CEP, while the anomalous precipitation in the MC region is further suppressed due to the adjustment of Walker circulation (Fig. 9b). The weakening convection corresponds to diminished cloud cover, allowing more SWR to penetrate the ocean surface and exacerbating the SST warming.

Anomalous LHF in JJ(1). Comparable to the equatorial CP, the changes in LHF anomalies are predominantly driven by atmospheric forcing (Fig. S15a and c), and the wind-induced LHF anomalies highly resemble the original LHF anomalies (Fig. S15e). For the JJ(1) period, the impact of wind changes on LHF anomalies can be decomposed into the contribution from the changes of climatological winds and wind anomalies (Fig. S16), revealing the predominant influence of the latter. During the CO₂ RD period, in contrast to the RU period, the positive precipitation anomalies around the MC region are intensified due to the increased Indo-Pacific zonal SST gradient (Fig. 2a, c), accompanied by the anomalous lower-level convergence and northerly anomalies (Fig. 9d), which partly offset the climatological southeasterly winds (Fig. 9c) and are conducive to SST warming by reducing evaporation

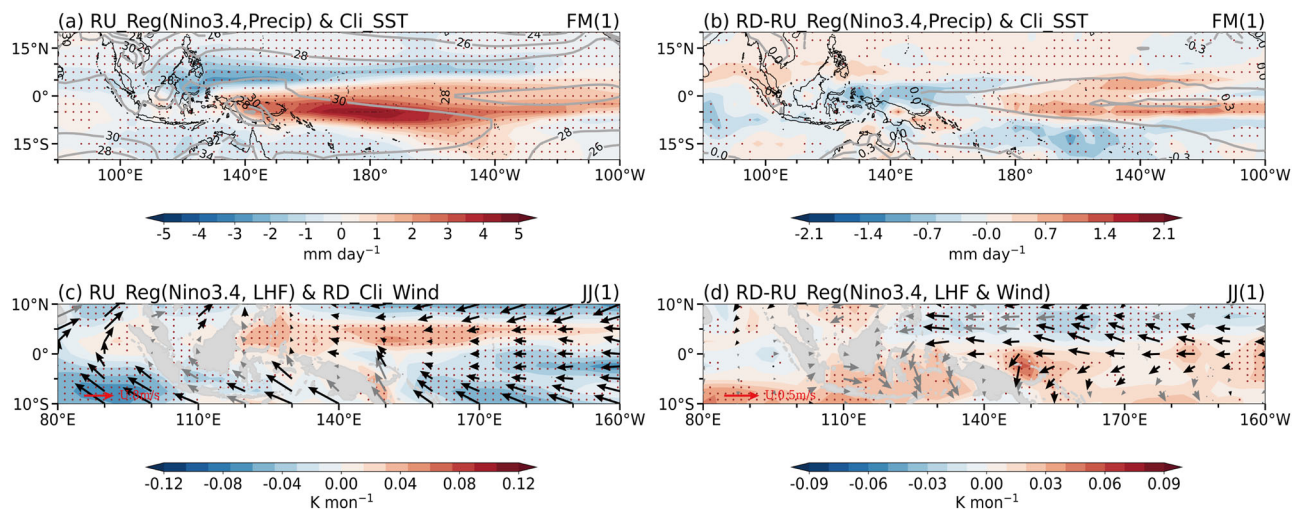


Fig. 9 | The spatial field corresponding to the key physical processes of the MC. **a** Climatological mean SST (contours; unit: °C) during FM(1) and regressed precipitation anomalies (shading; unit: mm day⁻¹) during FM(1) onto the standardized D(0)JF(1) Niño-3.4 index in the CO₂ RU period for 5 models' MME. **b** Same as (a), but for the differences between the CO₂ RD and RU period. The climatological mean SST is adjusted by subtracting the mean value across the entire tropics (20°S–20°N, 180°W–180°E). **c** Regressed LHF anomalies (shaded; unit: K month⁻¹) during JJ(1)

onto the standardized D(0)JF(1) Niño-3.4 index in the CO₂ RU period and climatological mean winds (vectors; unit: m s⁻¹) in the CO₂ RD period for 5 models' MME. **d** Regressed LHF anomalies (shaded; unit: K month⁻¹) and wind anomalies (vectors; unit: m s⁻¹) during JJ(1) onto the standardized D(0)JF(1) Niño-3.4 index in the differences between the CO₂ RD and RU period for 5 models' MME. Black arrows and brown dots denote that at least 70% of models show consistent results.

from ocean. Thus, a positive feedback emerges between local SST and LHF.

Discussion

The present study, based on CMIP6 models with idealized variations in CO₂ concentrations, delves into the asymmetric response of the WNPAC during post-ENSO summer and its underlying physical mechanisms. Our findings reveal a progressive strengthening of the anomalous WNPAC with the increase of CO₂ concentrations, and the intensification persists even as the CO₂ concentrations begin to decline, followed by a gradual recovery. The WNPAC fails to restore to its initial state when CO₂ concentrations return to PI level. Moreover, during the CO₂ RD phase, the pronounced asymmetric response of the WNPAC is likely to exacerbate the climate risks across East Asia, particularly with heightened temperature anomalies from the Indo-China Peninsula to the Philippines (Fig. S17b) and increased precipitation anomalies from central China to southern Japan (Fig. S17d). This asymmetric evolutionary characteristic of WNPAC can be explained by the variations of Indo-Pacific zonal SST gradient.

In contrast to the CO₂ RU period, the increased zonal SST gradient associated with the strengthened SST warming in the MC and the accelerated decay of positive SST anomalies in the equatorial CP is witnessed in the CO₂ RD period and favors the anomalous convection over the MC, which modulates the anomalous anticyclone through the Kelvin wave-induced Ekman divergence mechanism or the adjustment of meridional circulation within the local Hadley circulation. Additionally, the rapid decay of the equatorial CP SST anomalies weakens boundary layer moist enthalpy anomalies, which are transported by the climatological easterlies, enhancing moist stability over the WNP, suppressing local convection, and reinforcing the anticyclone as a Rossby wave response. The increased zonal SST gradient over the Indo-Pacific sector is ultimately stemming from the climatological equatorial Pacific El Niño-like warming pattern.

For the equatorial CP, the accelerated decay of SST anomalies is evident in late winter and early summer. In the late winter, the climatological equatorial Pacific warming is beneficial for the enhanced precipitation anomalies in the equatorial CP, thereby reducing the downward SWR by increasing cloud cover and exacerbates the LHF release through the intensified climatological northerly winds owing to the anomalous low-level wind convergence. Subsequently, in the early summer, the attenuation of the

climatological easterlies in the CP, related to the climatological equatorial Pacific warming, diminishes the meridional ocean currents on both sides of the equator; together with that the accelerated decay in local SST decrease the meridional temperature gradient, weakening of the meridional temperature advection and thus further exacerbating SST decline.

Concerning the MC, the downward SWR in the early spring is increased as that the local convection is suppressed due to that the climatological equatorial Pacific warming amplifies El Niño's influence on the anomalous weakened Walker circulation. During the early summer, the increased Indo-Pacific zonal SST gradient favors the positive precipitation anomalies corresponding with the anomalous lower-level wind convergence, which is opposite to the climatological southerly winds and reduces the LHF release, indicating a positive feedback between local SST and LHF. All the key processes and mechanisms are summarized in a schematic diagram (Fig. S18).

Under the CDR scenario, the upper ocean begins to cool rapidly, while the deep ocean continues to warm due to its huge heat capacity and the slow ocean dynamical processes^{38,77,78}. These weaken the vertical temperature gradient of the ocean and mitigates the cold upwelling efficiency in the equatorial CEP, thereby leading to an El Niño-like warming^{35,44,45,48}. Furthermore, the El Niño-like warming interacts with the slow recovery of walker circulation, which in turn contribute to the warming through Bjerknes feedback of air-sea coupling processes⁵¹. However, two fast processes, as non-uniform changes in evaporative patterns and cloud cover variations over the western Pacific, act to weaken the zonal SST contrast across the tropical Pacific and indirectly favor the El Niño-like warming under global warming scenario^{74,79}, and these processes are unlikely to operate in CDR scenario. The climatological El Niño-like warming causes the asymmetric response of the SST anomalies in the MC and equatorial CP during the El Niño decaying summer relative to variations in CO₂ concentrations. However, the peak occurrence times of these anomalies in the two regions are asynchronous, and the SST anomalies in the MC show a more discernible lag recovery compared to those in the equatorial CP. Further analysis reveals the importance of asynchronous response in the two regions' winter precipitation (Figs. 6c and 8c), which may include multifaceted processes at varying scales and complex mechanisms. Consequently, a comprehensive understanding of these dynamics necessitates further investigation, promising avenues for future research endeavors.

Methods

CMIP6

In this study, we utilize the 1pctCO2 and 1pctCO2-cdr experiments from the CMIP6. The 1pctCO2 experiment, spanning 150 years, features that CO₂ concentrations increase at a rate of 1% per year from the PI level (284.7 ppm). By the 140th year, CO₂ concentrations quadruple from the PI baseline, reaching 1138.8 ppm. The 1pctCO2-cdr experiment involves the symmetric removal of CO₂ over 140 years, followed by stabilization at the PI level for at least an additional 60 years. We extract data from years 1–140 of the 1pctCO2 experiment and years 1–200 of the 1pctCO2-cdr experiment to construct ideal CO₂ RU and RD scenarios. In these scenarios, CO₂ concentrations increase from year 1 to year 140, then decrease symmetrically from year 141 to year 280, and eventually stabilizes from year 281 to 340.

The ensemble for these experiments comprises nine models: ACCESS-ESM1-5, CanESM5, CAS-ESM2-0, CESM2, CNRM-ESM2-1, GFDL-ESM4, MIROC-ES2L, NorESM1-LM, and UKESM1-0-LL. For the analysis of atmospheric variables and SST, monthly outputs from all nine models are included in the calculations. However, for the analysis of the moisture budget, MSE budget and mixed-layer temperature tendency equation, CAS-ESM2-0, CESM2, GFDL-ESM4, and UKESM1-0-LL are excluded due to insufficient variables.

Data preprocessing and definition

All model datasets are interpolated onto a uniform 2.5° × 2.5° grid. To isolate interannual signals for evaluating variables' response to ENSO, an 8-year high-pass filter is applied to remove trends and interdecadal signals. Interannual anomalies are computed by subtracting the climatological mean over the entire time period. Following this, variable anomalies are regressed against the standardized Niño-3.4 index (defined as the SST anomalies averaged over 5°S–5°N, 120°–170°W during D(0)JF(1)) over a 51-year moving window. These regressions are carried out individually for each model, followed by averaging of all models to establish the MME, which serves to minimize model biases. In this study, the consensus among individual models is considered significant if at least 70% models agree on the sign⁸⁰. To ensure clarity and consistency, the 95% confidence intervals for the time evolution of all variables have been added and are presented collectively in Fig. S19.

Moisture budget

To analyze precipitation anomalies, the moisture budget approach is widely used⁸¹. The equation used to describe the ENSO-induced precipitation changes is presented as follows:

$$\Delta P' \approx \Delta E' - \Delta \langle \bar{u} \cdot \nabla_h q' \rangle - \Delta \langle \bar{u}' \cdot \nabla_h \bar{q} \rangle - \Delta \langle \bar{\omega} \cdot \partial_p q' \rangle - \Delta \langle \omega' \cdot \partial_p \bar{q} \rangle + NL. \quad (1)$$

In this formulation, Δ signifies the changes observed during the CO₂ RD period relative to the CO₂ RU period. The prime symbol indicates anomalies attributable to ENSO, and the overbar represents the climatological mean. The variables P , E , \bar{u} , q , and ω correspond to precipitation, evaporation, horizontal wind, specific humidity, and vertical pressure, respectively. The subscript h refers to the horizontal direction, and the subscript p corresponds to pressure. The NL indicates the sum of all non-linear terms. Each term on the right side of the equation, except for the evaporation term, can be further divided, and Eq. (1) can be expressed as follows⁸²:

$$\Delta P' \approx \Delta E' - \langle \Delta \bar{u} \cdot \nabla_h q' \rangle - \langle \Delta \bar{u}' \cdot \nabla_h (\Delta \bar{q}) \rangle - \langle \Delta \bar{\omega}' \cdot \partial_p \bar{q} \rangle - \langle \bar{\omega}' \cdot \partial_p (\Delta \bar{q}) \rangle$$

$$- \langle \Delta \bar{\omega} \cdot \partial_p q' \rangle - \langle \bar{\omega} \cdot \partial_p (\Delta q') \rangle - \langle \Delta \omega' \cdot \partial_p \bar{q} \rangle - \langle \omega' \cdot \partial_p (\Delta \bar{q}) \rangle + NL. \quad (2)$$

MSE budget

In the tropics, the vertical motion is largely controlled by the MSE budget⁸³. The MSE equation is represented as follows:

$$\partial_t \langle s' \rangle + \langle \bar{u} \cdot \nabla_h s' \rangle + \langle \omega \cdot \partial_p h' \rangle = F'_{net}. \quad (3)$$

MSE is defined as $h = c_p T + L_v q + gz$, with $s = c_p T + L_v q$ representing the moist enthalpy. The variables T and z refer to atmospheric temperature, and geopotential height, respectively, while F'_{net} indicates the net MSE flux. The constants c_p , L_v , and g denote the specific heat at constant pressure, the latent heat of vaporization, and gravitational acceleration, respectively. The time tendency term $\partial_t \langle s' \rangle$ is considered negligible over interannual timescales. Changes in the MSE equation between CO₂ RD and CO₂ RU period can be expressed as⁸²:

$$\begin{aligned} \langle \Delta \omega' \cdot \partial_p \bar{h} \rangle &\approx - \langle \omega' \cdot \partial_p (\Delta \bar{h}) \rangle + \Delta F'_{net} \\ &- \langle \Delta \bar{u} \cdot \nabla_h s' \rangle - \langle \Delta \bar{u}' \cdot \nabla_h (\Delta s') \rangle \\ &- \langle \Delta \bar{u}' \cdot \nabla_h \bar{s} \rangle - \langle \bar{u}' \cdot \nabla_h (\Delta \bar{s}) \rangle \\ &- \langle \Delta \bar{\omega} \cdot \partial_p h' \rangle - \langle \bar{\omega} \cdot \partial_p (\Delta h') \rangle + NL, \end{aligned} \quad (4)$$

where the net MSE flux, F'_{net} , entering an atmospheric column encompasses contributions from both the top and the surface of the atmosphere:

$$F'_{net} = (S_t^\downarrow - S_t^\uparrow - R_t^\uparrow) - (-S_s^\uparrow + S_s^\downarrow - R_s^\uparrow + R_s^\downarrow - LH - SH). \quad (5)$$

The first three terms (S_t^\downarrow , S_t^\uparrow , R_t^\uparrow) represent radiative fluxes entering an atmospheric column from the top of the atmosphere, including downward shortwave, upward shortwave, and upward longwave radiative fluxes. The following six terms (S_s^\uparrow , S_s^\downarrow , R_s^\uparrow , R_s^\downarrow , LH , SH) describe fluxes entering from the surface, comprising both shortwave and longwave radiative fluxes in both directions, as well as latent and sensible heat fluxes. Positive values in this context indicate atmospheric heating.

Mixed-layer temperature tendency equation

We employ a diagnostic equation for the mixed-layer energy balance to identify the dominant contribution of thermodynamic and dynamic processes to the SST anomalies in the equatorial CP and MC. The mixed-layer temperature tendency equation is expressed as:

$$\frac{\partial T'}{\partial t} = - \left(u' \frac{\partial \bar{T}}{\partial x} + v' \frac{\partial \bar{T}}{\partial y} + w' \frac{\partial \bar{T}}{\partial z} \right) - \left(\bar{u} \frac{\partial T'}{\partial x} + \bar{v} \frac{\partial T'}{\partial y} + \bar{w} \frac{\partial T'}{\partial z} \right) + \frac{Q'_{net}}{\rho C_p H} + R \quad (6)$$

Here, a prime represents the anomaly caused by ENSO, and a bar represents the climatological mean. T denotes the mixed-layer potential temperature, and $\partial T / \partial t$ indicates its tendency. $-(u' \frac{\partial \bar{T}}{\partial x} + v' \frac{\partial \bar{T}}{\partial y} + w' \frac{\partial \bar{T}}{\partial z}) - (\bar{u} \frac{\partial T'}{\partial x} + \bar{v} \frac{\partial T'}{\partial y} + \bar{w} \frac{\partial T'}{\partial z})$ denotes ocean dynamic terms (D), u , v , and w are three-dimensional ocean currents. $\frac{Q'_{net}}{\rho C_p H}$ denotes ocean thermodynamic term (Q). $Q_{net} = SWR + LWR + SHF + LHF$ is the net surface heat flux, in which SWR is the net surface shortwave radiation flux, LWR is the net surface longwave radiation flux, SHF is the surface sensible heat flux, and

LHF is the surface latent heat flux. All these heat fluxes are downward positive, corresponding to ocean warming. $\rho = 10^3 \text{ kg m}^{-3}$ is the density of seawater, and $C_p = 4000 \text{ J kg}^{-1} \text{ K}^{-1}$ is the specific heat of ocean. H is the depth of the mixed layer, and H is set as a constant 50 meters for simplicity, following the precedent set in a previous studies^{36,84–86}. R represents the residual term. The nonlinear terms have a negligible effect on the SST anomalies over the equatorial CP and MC, so these terms are disregarded in our analysis.

The decomposition of the LHF anomalies

The LHF anomalies can be decomposed into components of oceanic response and atmospheric forcing, denoted as Q'_{Ocean} and Q'_{Air} respectively. Q'_{Air} primarily encompasses the effects of relative humidity (Q'_{RH}), wind speed (Q'_{Wind}), and sea-air temperature difference (Q'_T). Following ref. 87, the individual contribution of these factors can be expressed as:

$$Q'_{\text{Ocean}} = \overline{\text{LHF}} \left(\frac{1}{\bar{q}_s} \frac{dq'_s}{dT} \right) T' \quad (7)$$

$$Q'_{\text{Air}} = \text{LHF}' - Q'_{\text{Ocean}} \quad (8)$$

$$Q'_{\text{Wind}} = \overline{\text{LHF}} \frac{W'}{W} \quad (9)$$

$$Q'_{\text{RH}} = \overline{\text{LHF}} \frac{\text{RH}'}{\overline{\text{RH}}} \quad (10)$$

$$Q'_T = \overline{\text{LHF}} \frac{\Delta T'}{\Delta \bar{T}} \quad (11)$$

where the overbar and prime symbols represent the climatological mean and the anomaly caused by ENSO, respectively. q_s denotes the saturated specific humidity following the Clausius-Clapeyron equation. W stands for surface wind speed. RH refers to surface relative humidity. T represents SST, and ΔT is the temperature difference between SST and near-surface air temperature. Due to the limited availability of near-surface atmospheric variables in model outputs, the 1000-hPa winds and relative humidity are used for instead.

The changes of wind-induced LHF anomalies can be decomposed as:

$$\Delta Q'_{\text{Wind}} = \Delta \frac{\overline{\text{LHF}}}{W} W' + \frac{\overline{\text{LHF}}}{W} \Delta W' \quad (12)$$

$\Delta \frac{\overline{\text{LHF}}}{W} W'$ and $\frac{\overline{\text{LHF}}}{W} \Delta W'$ represent the contribution of the climatological mean and anomalous wind speed, respectively.

Data availability

The CMIP6 outputs are available online on <https://esgf-node.llnl.gov/projects/cmip6/>.

Received: 25 June 2024; Accepted: 4 December 2024;

Published online: 20 December 2024

References

- Chang, C. P., Zhang, Y. & Li, T. Interannual and interdecadal variations of the East Asian summer monsoon and tropical Pacific SSTs. Part I: Roles of the subtropical ridge. *J. Clim.* **13**, 4310–4325 (2000).
- Wang, B., Wu, R. G. & Fu, X. H. Pacific-East Asian teleconnection: How does ENSO affect East Asian climate? *J. Clim.* **13**, 1517–1536 (2000).
- Hu, K. M., Huang, G. & Huang, R. H. The impact of tropical Indian Ocean variability on summer surface air temperature in China. *J. Clim.* **24**, 5365–5377 (2011).
- Zhang, R. H., Min, Q. Y. & Su, J. Z. Impact of El Niño on atmospheric circulations over East Asia and rainfall in China: Role of the anomalous western North Pacific anticyclone. *Sci. China: Earth Sci.* **60**, 1124–1132 (2017).
- Klein, S. A., Soden, B. J. & Lau, N. C. Remote sea surface temperature variations during ENSO: Evidence for a tropical atmospheric bridge. *J. Clim.* **12**, 917–932 (1999).
- Alexander, M. A. et al. The atmospheric bridge: The influence of ENSO teleconnections on air-sea interaction over the global oceans. *J. Clim.* **15**, 2205–2231 (2002).
- Xie, S. P., Annamalai, H., Schott, F. A. & McCreary, J. P. Structure and mechanisms of South Indian Ocean climate variability. *J. Clim.* **15**, 864–878 (2002).
- Du, Y., Xie, S. P., Huang, G. & Hu, K. M. Role of air-sea interaction in the long persistence of El Niño-induced north Indian Ocean warming. *J. Clim.* **22**, 2023–2038 (2009).
- Yang, J. L., Liu, Q. Y., Xie, S. P., Liu, Z. Y. & Wu, L. X. Impact of the Indian Ocean SST basin mode on the Asian summer monsoon. *Geophys. Res. Lett.* **34**, L02708 (2007).
- Wu, B., Zhou, T. J. & Li, T. Seasonally evolving dominant interannual variability modes of East Asian climate. *J. Clim.* **22**, 2992–3005 (2009).
- Xie, S. P. et al. Indian Ocean capacitor effect on Indo-western Pacific climate during the summer following El Niño. *J. Clim.* **22**, 730–747 (2009).
- Huang, G., Hu, K. M. & Xie, S. P. Strengthening of tropical Indian Ocean teleconnection to the northwest Pacific since the mid-1970s: An atmospheric GCM study. *J. Clim.* **23**, 5294–304 (2010).
- Wu, B., Li, T. & Zhou, T. J. Relative contributions of the Indian Ocean and local SST anomalies to the maintenance of the western North Pacific anomalous anticyclone during the El Niño decaying summer. *J. Clim.* **23**, 2974–2986 (2010).
- Xiang, B. Q., Wang, B., Yu, W. D. & Xu, S. B. How can anomalous western North Pacific subtropical high intensify in late summer? *Geophys. Res. Lett.* **40**, 2349–2354 (2013).
- Wang, Y., Wu, B. & Zhou, T. Maintenance of western North Pacific anomalous anticyclone in boreal summer by wind-induced moist enthalpy advection mechanism. *J. Clim.* **35**, 4499–4511 (2022).
- Chen, X. L. & Zhou, T. J. Relative role of tropical SST forcing in the 1990s periodicity change of the Pacific-Japan pattern interannual variability. *J. Geophys. Res.: Atmos.* **119**, 13043–13066 (2014).
- Tao, W. C. et al. Asymmetry in summertime atmospheric circulation anomalies over the northwest Pacific during decaying phase of El Niño and La Niña. *Clim. Dyn.* **49**, 2007–2023 (2017).
- Tao, W. C. et al. Dominant modes of CMIP3/5 models simulating northwest Pacific circulation anomalies during post-ENSO summer and their SST dependence. *Theor. Appl. Climatol.* **138**, 1809–1820 (2019).
- Xie, S. P. et al. Indo-western Pacific ocean capacitor and coherent climate anomalies in post-ENSO summer: A review. *Adv. Atmos. Sci.* **33**, 411–432 (2016).
- Wang, B., Xiang, B. Q. & Lee, J. Y. Subtropical high predictability establishes a promising way for monsoon and tropical storm predictions. *Proc. Natl Acad. Sci.* **110**, 2718–2722 (2013).
- Jiang, W. P. et al. Northwest Pacific anticyclonic anomalies during post-El Niño summers determined by the pace of El Niño decay. *J. Clim.* **32**, 3487–3503 (2019).
- Tao, W. C., Kong, X. W., Liu, Y., Wang, Y. & Dong, D. H. Diversity of Northwest Pacific atmospheric circulation anomalies during post-ENSO summer. *Front. Environ. Sci.* **10**, 1068155 (2022).
- Chung, P. H., Sui, C. H. & Li, T. Interannual relationships between the tropical sea surface temperature and summertime subtropical anticyclone over the western North Pacific. *J. Geophys. Res.: Atmos.* **116**, D13111 (2011).

24. Lane, J. E., Kruuk, L. E. B., Charmanier, A., Murie, J. O. & Dobson, F. S. Delayed phenology and reduced fitness associated with climate change in a wild hibernator. *Nature* **489**, 554–557 (2012).
25. Richardson, A. D. et al. Ecosystem warming extends vegetation activity but heightens vulnerability to cold temperatures. *Nature* **560**, 368–371 (2018).
26. Kotz, M., Lange, S., Wenz, L. & Levermann, A. Constraining the pattern and magnitude of projected extreme precipitation change in a multi-model ensemble. *J. Clim.* **37**, 97–111 (2023).
27. Peters, G. P. et al. The challenge to keep global warming below 2 °C. *Nat. Clim. Change* **3**, 4–6 (2013).
28. Keller, D. P. et al. The carbon dioxide removal model intercomparison project (CDRMIP): Rationale and experimental protocol for CMIP6. *Geosci. Model Dev.* **11**, 1133–60 (2018).
29. Rogelj, J. et al. Scenarios towards limiting global mean temperature increase below 1.5 °C. *Nat. Clim. Change* **8**, 325–332 (2018).
30. Realmonde, G. et al. An inter-model assessment of the role of direct air capture in deep mitigation pathways. *Nat. Commun.* **10**, 3277 (2019).
31. Wu, P., Ridley, J., Pardaens, A., Levine, R. & Lowe, J. The reversibility of CO₂ induced climate change. *Clim. Dyn.* **45**, 745–754 (2015).
32. Kim, S.-K. et al. Widespread irreversible changes in surface temperature and precipitation in response to CO₂ forcing. *Nat. Clim. Chang.* **12**, 834–840 (2022).
33. Wu, P., Wood, R., Ridley, J. & Lowe, J. Temporary acceleration of the hydrological cycle in response to a CO₂ rampdown. *Geophys. Res. Lett.* **37**, L12705 (2010).
34. Chadwick, R., Wu, P., Good, P. & Andrews, T. Asymmetries in tropical rainfall and circulation patterns in idealised CO₂ removal experiments. *Clim. Dyn.* **40**, 295–316 (2013).
35. Song, S.-Y. et al. Climate sensitivity controls global precipitation hysteresis in a changing CO₂ pathway. *npj Clim. Atmos. Sci.* **6**, 1–10 (2023).
36. Zhou, S. J., Huang, P., Xie, S. P., Huang, G. & Wang, L. Varying contributions of fast and slow responses cause asymmetric tropical rainfall change between CO₂ ramp-up and ramp-down. *Sci. Bull.* **67**, 1702–1711 (2022).
37. Boucher, O. et al. Reversibility in an Earth System model in response to CO₂ concentration changes. *Environ. Res. Lett.* **7**, 024013 (2012).
38. Long, S. M. et al. Effects of ocean slow response under low warming targets. *J. Clim.* **33**, 477–496 (2020).
39. Garbe, J., Albrecht, T., Levermann, A., Donges, J. F. & Winkelmann, R. The hysteresis of the Antarctic ice sheet. *Nature* **585**, 538–544 (2020).
40. Kug, J. S. et al. Hysteresis of the intertropical convergence zone to CO₂ forcing. *Nat. Clim. Change* **12**, 47–53 (2022).
41. An, S.-I. et al. General circulation and global heat transport in a quadrupling CO₂ pulse experiment. *Sci. Rep.* **12**, 11569 (2022).
42. Kim, S. Y. et al. Hemispherically asymmetric Hadley cell response to CO₂ removal. *Sci. Adv.* **9**, eadg1801 (2023).
43. Sun, M.-A. et al. Reversibility of the hydrological response in East Asia from CO₂-derived climate change based on CMIP6 simulation. *Atmosphere* **12**, 72 (2021).
44. Song, S. Y. et al. Asymmetrical response of summer rainfall in East Asia to CO₂ forcing. *Sci. Bull.* **67**, 213–222 (2022).
45. Zhang, S. Q., Qu, X., Huang, G. & Hu, P. Asymmetric response of South Asian summer monsoon rainfall in a carbon dioxide removal scenario. *npj Clim. Atmos. Sci.* **6**, 10 (2023).
46. Zhang, S. et al. Delayed onset of Indian summer monsoon in response to CO₂ removal. *Earth's Future* **12**, e2023EF004039 (2024).
47. An, S. I. et al. Intensity changes of Indian Ocean dipole mode in a carbon dioxide removal scenario. *npj Clim. Atmos. Sci.* **5**, 20 (2022).
48. Ohba, M., Tsutsui, J. & Nohara, D. Statistical parameterization expressing ENSO variability and reversibility in response to CO₂ concentration changes. *J. Clim.* **27**, 398–410 (2014).
49. Liu, C. et al. Hysteresis of the El Niño–Southern Oscillation to CO₂ forcing. *Sci. Adv.* **9**, eadh8442 (2023).
50. Liu, C. et al. ENSO skewness hysteresis and associated changes in strong El Niño under a CO₂ removal scenario. *npj Clim. Atmos. Sci.* **6**, 1–10 (2023).
51. Kim, G.-I. et al. Deep ocean warming-induced El Niño changes. *Nat. Commun.* **15**, 6225 (2024).
52. Liu, C. et al. Hemispheric asymmetric response of tropical cyclones to CO₂ emission reduction. *npj Clim. Atmos. Sci.* **7**, 1–11 (2024).
53. Jiang, W. P., Huang, G., Huang, P. & Hu, K. M. Weakening of northwest Pacific anticyclone anomalies during post-El Niño summers under global warming. *J. Clim.* **31**, 3539–3555 (2018).
54. He, C., Cui, Z. Y. & Wang, C. Z. Response of western North Pacific anomalous anticyclones in the summer of decaying El Niño to global warming: Diverse projections based on CMIP6 and CMIP5 models. *J. Clim.* **35**, 359–372 (2022).
55. Wu, M. N., Zhou, T. J. & Chen, X. L. The source of uncertainty in projecting the anomalous western North Pacific anticyclone during El Niño–decaying summers. *J. Clim.* **34**, 6603–6617 (2021).
56. Yeh, S. W. & Kirtman, B. P. ENSO amplitude changes due to climate change projections in different coupled models. *J. Clim.* **20**, 203–217 (2007).
57. Collins, M. et al. The impact of global warming on the tropical Pacific Ocean and El Niño. *Nat. Geosci.* **3**, 391–397 (2010).
58. Cai, W. J. et al. ENSO and greenhouse warming. *Nat. Clim. Change* **5**, 849–859 (2015).
59. Tao, W. C. et al. Interdecadal modulation of ENSO teleconnections to the Indian Ocean Basin Mode and their relationship under global warming in CMIP5 models. *Int. J. Climatol.* **35**, 391–407 (2015).
60. Hu, K. M. et al. Interdecadal variations in ENSO influences on northwest Pacific–East Asian early summertime climate simulated in CMIP5 models. *J. Clim.* **27**, 5982–5998 (2014).
61. Zheng, X. T., Xie, S. P. & Liu, Q. Y. Response of the Indian Ocean basin mode and its capacitor effect to global warming. *J. Clim.* **24**, 6146–6164 (2011).
62. Chen, W., Lee, J. Y., Ha, K. J., Yun, K. S. & Lu, R. Y. Intensification of the western North Pacific anticyclone response to the short decaying El Niño event due to greenhouse warming. *J. Clim.* **29**, 3607–3627 (2016).
63. Gill, A. E. Some simple solutions for heat-induced tropical circulation. *Q. J. R. Meteorol. Soc.* **106**, 447–462 (1980).
64. Wu, B., Zhou, T. & Li, T. Atmospheric dynamic and thermodynamic processes driving the western North Pacific anomalous anticyclone during El Niño. Part I: Maintenance mechanisms. *J. Clim.* **30**, 9621–9635 (2017).
65. Xie, S. P. et al. Decadal shift in El Niño influences on Indo-western Pacific and East Asian climate in the 1970s. *J. Clim.* **23**, 3352–3368 (2010).
66. Roca, R., Viollier, M., Picon, L. & Desbois, M. A multisatellite analysis of deep convection and its moist environment over the Indian Ocean during the winter monsoon. *J. Geophys. Res. Atmos.* **107**, 11–25 (2002).
67. Huang, P. & Xie, S. P. Mechanisms of change in ENSO-induced tropical Pacific rainfall variability in a warming climate. *Nat. Geosci.* **8**, 922–926 (2015).
68. Ramanathan, V. & Collins, W. Thermodynamic regulation of ocean warming by cirrus clouds deduced from observations of the 1987 El Niño. *Nature* **351**, 27–32 (1991).
69. Ying, J. & Huang, P. Cloud–radiation feedback as a leading source of uncertainty in the tropical Pacific SST warming pattern in CMIP5 models. *J. Clim.* **29**, 3867–3881 (2016).
70. Fu, R., Liu, W. T. & Dickinson, R. E. Response of tropical clouds to the interannual variation of sea surface temperature. *J. Clim.* **9**, 616–634 (1996).
71. Meenu, S., Parameswaran, K. & Rajeev, K. Role of sea surface temperature and wind convergence in regulating convection over the tropical Indian Ocean. *J. Geophys. Res.* **117**, D14102 (2012).

72. Meehl, G. A. & Washington, W. M. El Niño-like climate change in a model with increased atmospheric CO₂ concentrations. *Nature* **382**, 56–60 (1996).
73. Tokinaga, H., Xie, S. P., Deser, C., Kosaka, Y. & Okumura, Y. M. Slowdown of the Walker circulation driven by tropical Indo-Pacific warming. *Nature* **491**, 439–443 (2012).
74. Ying, J., Huang, P. & Huang, R. H. Evaluating the formation mechanisms of the equatorial Pacific SST warming pattern in CMIP5 models. *Adv. Atmos. Sci.* **33**, 433–441 (2016).
75. Chen, L., Li, T., Yu, Y. Q. & Behera, S. K. A possible explanation for the divergent projection of ENSO amplitude change under global warming. *Clim. Dyn.* **49**, 3799–3811 (2017).
76. Yan, Z. X. et al. Eastward shift and extension of ENSO-induced tropical precipitation anomalies under global warming. *Sci. Adv.* **6**, eaax4177 (2020).
77. Held, I. M. et al. Probing the fast and slow components of global warming by returning abruptly to preindustrial forcing. *J. Clim.* **23**, 2418–2427 (2010).
78. Long, S.-M., Xie, S.-P., Zheng, X.-T. & Liu, Q. Fast and slow responses to global warming: Sea surface temperature and precipitation patterns. *J. Clim.* **27**, 285–299 (2014).
79. DiNezio, P. N. et al. Climate response of the equatorial Pacific to global warming. *J. Clim.* **22**, 4873–4892 (2009).
80. Power, S. B., Delage, F., Colman, R. & Moise, A. Consensus on twenty-first-century rainfall projections in climate models more widespread than previously thought. *J. Clim.* **25**, 3792–3809 (2012).
81. Chou, C. et al. Increase in the range between wet and dry season precipitation. *Nat. Geosci.* **6**, 263–267 (2013).
82. Sun, N. et al. Amplified tropical Pacific rainfall variability related to background SST warming. *Clim. Dyn.* **54**, 2387–2402 (2020).
83. Neelin, J. D. & Held, I. M. Modeling tropical convergence based on the moist static energy budget. *Mon. Weather Rev.* **115**, 3–12 (1987).
84. Tang, H. S. et al. Weak persistence of Northwest Pacific anomalous anticyclone during post-El Niño summers in CMIP5 and CMIP6 models. *Clim. Dyn.* **61**, 3805–3830 (2023).
85. Tao, W. C. et al. Origins of biases in CMIP5 models simulating northwest Pacific summertime atmospheric circulation anomalies during the decaying phase of ENSO. *J. Clim.* **31**, 5707–5729 (2018).
86. Wang, B. et al. Historical change of El Niño properties sheds light on future changes of extreme El Niño. *Proc. Natl Acad. Sci. USA* **116**, 22512–22517 (2019).
87. Du, Y. & Xie, S. P. Role of atmospheric adjustments in the tropical Indian Ocean warming during the 20th century in climate models. *Geophys. Res. Lett.* **35**, L08712 (2008).

Acknowledgements

We acknowledge the World Climate Research Program, which coordinated and promoted CMIP6 through its Working Group on Coupled Modelling. This work is supported by the National Natural Science Foundation of China (Grant Nos. 42141019, 42261144687, 42475048, 42175049, 42405041, and 42105032).

Author contributions

W.Z. and W.T. conceived the study, performed the analyses, and wrote the paper. All authors participated in discussing and revising the paper.

Competing interests

The authors declare no competing interests.

Additional information

Supplementary information The online version contains supplementary material available at

<https://doi.org/10.1038/s41612-024-00871-3>.

Correspondence and requests for materials should be addressed to Weichen Tao or Gang Huang.

Reprints and permissions information is available at <http://www.nature.com/reprints>

Publisher's note Springer Nature remains neutral with regard to jurisdictional claims in published maps and institutional affiliations.

Open Access This article is licensed under a Creative Commons Attribution-NonCommercial-NoDerivatives 4.0 International License, which permits any non-commercial use, sharing, distribution and reproduction in any medium or format, as long as you give appropriate credit to the original author(s) and the source, provide a link to the Creative Commons licence, and indicate if you modified the licensed material. You do not have permission under this licence to share adapted material derived from this article or parts of it. The images or other third party material in this article are included in the article's Creative Commons licence, unless indicated otherwise in a credit line to the material. If material is not included in the article's Creative Commons licence and your intended use is not permitted by statutory regulation or exceeds the permitted use, you will need to obtain permission directly from the copyright holder. To view a copy of this licence, visit <http://creativecommons.org/licenses/by-nc-nd/4.0/>.

© The Author(s) 2024